Multi-layer frozen profiler from single conjugated adaptive optics telemetry: novel approach and potential applications

Anthony Berdeu, Miguel Montargès, Jean-Baptiste Le Bouquin, Julien Woillez, Ferréol Soulez, Thibaut Paumard, Denis Defrère, Frank Eisenhauer, Paulo J. V. Garcia, Sebastian Hönig, et al.

Multi-layer frozen profiler from single conjugated adaptive optics telemetry: novel approach and potential applications

Anthony Berdeu[a,b], Miguel Montargès[b], Jean-Baptiste Le Bouquin[c], Julien Woillez[d], Ferréol Soulez[e], Thibaut Paumard[b], Frank Eisenhauer[f], Christian Straubmeier[g], Paulo Garcia[h,i], Sebastian Hönig[j], Florentin Millour[k], Laura Kreidberg[l], Denis Defrère[m], and GRAVITY+ Collaboration

[a]European Southern Observatory, Alonso de Cordova, 3107 Vitacura, Santiago, Chile
[b]LIRA, Observatoire de Paris, Université PSL, Sorbonne Université, Université Paris Cité, CY Cergy Paris Université, CNRS, 92190 Meudon, France
[c]Univ. Grenoble Alpes, CNRS, IPAG, 38000 Grenoble, France
[d]European Southern Observatory, Karl-Schwarzschild-Straße 2, 85748 Garching, Germany
[e]Univ Lyon, Univ Lyon1, Ens de Lyon, Centre de Recherche Astrophysique de Lyon, UMR 5574, F-69230, Saint-Genis-Laval, France
[f]Max Planck Institute for extraterrestrial Physics, 85748 Garching, Germany
[g]1st Institute of Physics, University of Cologne, Zülpicher Straße 77, 50937 Cologne, Germany
[h]Centro de Astrofísica e Gravitação, IST, Universidade de Lisboa, 1049-001 Lisboa, Portugal
[i]Faculdade de Engenharia, Universidade do Porto, 4200-465 Porto, Portugal
[j]School of Physics & Astronomy, University of Southampton, Southampton, SO17 1BJ, UK
[k]Université Côte d'Azur, Observatoire de la Côte d'Azur, CNRS, Laboratoire Lagrange, France
[l]Max Planck Institute for Astronomy, Königstuhl 17, 69117 Heidelberg, Germany
[m]Institute of Astronomy, KU Leuven, Celestijnenlaan 200D, B-3001, Leuven, Belgium

Send correspondence to Anthony Berdeu: anthony.berdeu@obspm.fr
The poster is uploaded as supplementary material.

ABSTRACT

New generations of adaptive optics (AO) systems give access to an unprecedented stream of data at spatial and temporal resolutions never before achieved for routine scientific operations. This is for example the case for the GRAVITY+ AO (GPAO) system upgrade: the four 8 meters units of the Very Large Telescope were equipped with 43x43 deformable mirrors (DM, 1432 actuators) as well as new 40x40 visible and 30x30 laser guide star Shack-Hartmann wavefront sensors. By its number of measures and controlled actuators, GPAO prefigures those of the AO systems of future giant telescopes. However, so far, the AO telemetry from these systems remains largely underexploited beyond pure real-time AO applications. In this work, we present a novel turbulence profiler working on single-conjugated AO telemetry (SCAO). Under the assumption that the atmosphere is composed of mixed frozen flow layers (but without assumption on their structure function), it jointly retrieves the individual wind speed, direction, and strength (Cn2 coefficient) of the main contributors to the turbulence. Only their height remains unknown as a result of the lack of stereoscopic information in SCAO systems. Our model successfully fits standard conditions at the Paranal Observatory, disentangling up to eight independent layers. Straightforwardly, it can be used to refine the atmospheric monitor of the real-time computer: Fried's parameters r0, t0, v0 or seeing and residual variances of AO. Our work shows that single-layer-frozen flow is not a realistic approximation for most situations and demonstrates that the dominant multi-layers can be effectively reconstructed from operational telemetry. As such, our method paves the way towards more transformative applications, such as (i) the debiasing of DM/WFS misregistration estimators based on AO telemetry whose performances are undermined by strong winds, or (ii) more excitingly, to a piston reconstructor, the ultimate limit of ground-based interferometers.

Keywords: AO telemetry ; Data analysis ; Inverse problem approach ; Physical modelling ; Wavefront reconstruction ; Wavefront prediction ; Atmospheric turbulence ; Frozen flow ; Kolmogorov ; Seeing ; Fried's parameter

1. INTRODUCTION

Early Adaptive Optics (AO) systems quickly highlighted the occurrence of frozen layers in the corrected turbulence [7, 8, 18]. Nonetheless, the limited resolution of the wavefront sensors (WFSs) prevented deeper analysing of the turbulence profile. With the recent increase of WFS resolution and performances of AO systems, we have now access to an unprecedented stream of data, both spatially and temporally. The GRAVITY+ Adaptive Optics system [GPAO, 9] is one of them, equipped with a 43×43 deformable mirror (DM, 1432 actuators) and multiple Shack-Hartmann wavefront sensors (SH-WFSs): a 40×40 SH-WFS for visible natural guide star (NGS VIS mode), a 9×9 SH-WFS for infra-red natural guide star (NGS IR mode) and a 30×30 laser guide star SH-WFS (LGS mode)*. To calibrate, control, and monitor the system, many modules have been developed and implemented in its Real Time Computer [RTC, 5, 21] and are the subject of another communication, see Ref. [3].

Among these different modules, the so-called `AtmPerfMonitor` is dedicated to the monitoring of the AO loop performances and the turbulence parameters. Inherited from the adaptive optics facility [AOF, 12], it initially provided the estimated seeing along with the Fried's parameter r_0 and outer scale L_0. Nonetheless, it was lacking of a wind estimator and consequently could not provide the coherence time τ_0 measured from the point of view of the AO system, a critical parameter for the downstream interferometers. In addition, GPAO implements a novel approach to measure and correct its lateral mis-alignment in operation with a non-perturbative approach based on closed loop telemetry [2]. These kinds of estimators are easily biased by the wind, see Ref. [10]. Even if GPAO does better, see Ref. [3], it is not spared in difficult conditions combining strong winds and slow frame rates. A quantitative wind estimator could help de-biasing the estimators or at least identify the situations that degrade their performances. Beyond GPAO, having an estimate of the equivalent wind speed and coherent time can help to understand the performances of the system, especially for extreme AO systems where wind drive halo (servo-lag errors) can dominate the residual stellar flux in high contrast imaging [15].

Different methods exist to retrieve the wind from AO telemetry, looking at pseudo-open loop correlations [15, 23] or their power spectrum density [7, 18]. If they work well on simulations with perfectly frozen layers that produce sharp signals, they encounter difficulties on real data where the inherent boiling and decorrelation blur and mix the signals [6].

In this work we present a novel approach to extract the velocity and strength of turbulent frozen layers. We start by re-defining the pseudo-open loop spatio-spectral auto-correlation cube to properly account for the pupil masking in Sec. 2.1. In Sec. 2.2, we present our method to disentangle the different layers from this cube, by estimating their 2D correlation maps in their full complexity rather than only focusing on their brightest

*There is a fourth 4×4 SH-WFS for low order correction in the LGS mode. But it is never used in standalone AO loops and is thus not considered in this work.

peaks as classically done. Then we present results of the method on real on-sky data with a complex turbulence profile in 3.1. Implemented in the `AtmPerfMonitor` of GPAO, our approach is now routinely used in operation and compared with Differential Image Motion Monitor (DIMM) data in Sec. 3.2 for all GPAO modes. Finally, in Sec. 3.3, we present the perspectives opened by this multi-layer frozen flow profiler regarding AO system auto-calibration and monitoring or even wavefront prediction.

2. METHODS

2.1 Pseudo-open Loop Weighted Auto-Correlation

Figure 1 presents the pseudo-open loop of on-sky telemetry recorded with GPAO in NGS VIS. They are obtained by combining the residual slopes measured by the 40×40 SH-WFS sensor with the pseudo interaction matrix model multiplied by the commands applied on the DM. The 2D slopes $\boldsymbol{s} = (s_x, s_y)$ are reshaped in the frame of the SH-WFS sub-apertures of 2D coordinates $\boldsymbol{\theta} = (\theta_x, \theta_y)$. Looking carefully at the maps, it is possible to see similar patterns that translates with time. Indicating that a part of the wavefront translates with the wind, this information should be easily identifiable in the $2\mathrm{D} + t$ correlations.

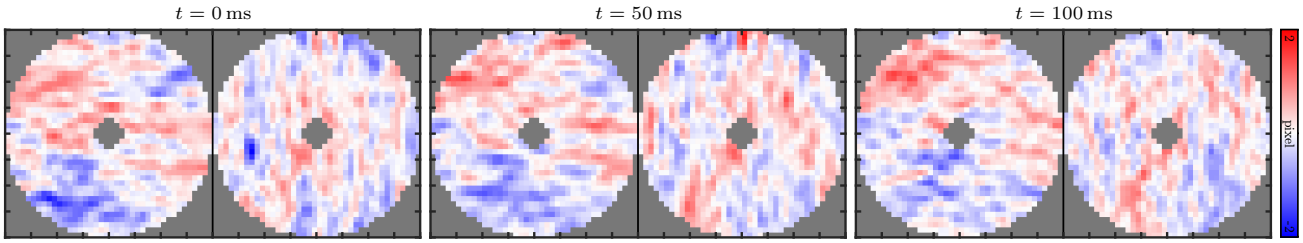

Figure 1. On-sky x (left) and y pseudo-open loop slopes at different timing measured by the 40×40 SH-WFS of the NGS VIS mode of GPAO. The gray area $p(\theta) = 0$ is outside the pupil mask. The different maps show similar patterns that are translated by the wind.

Most of the methods straightforwardly directly compute the auto-correlation of the temporal cube of the reshaped 2D slopes [6, 8, 17] without accounting for the fact that the slopes are only measured on the pupil mask

$$p(\boldsymbol{\theta}) = 1 \text{ if } \boldsymbol{\theta} \in \text{pupil and } 0 \text{ otherwise.} \tag{1}$$

Doing so biases the correlation for large 2D shifts $\boldsymbol{\delta}_\theta$ which tends towards zero. In this work, we consider the weighted auto-correlation of the pseudo-open loop slope cube computed as a similarity coefficient between the $2\mathrm{D} + t$ slope cube $\boldsymbol{s}(\boldsymbol{\theta}, t)$ and its version translated by $(\boldsymbol{\delta}_\theta, \delta_t)$,

$$\alpha(\boldsymbol{\delta}_\theta, \delta_t) = \underset{\beta}{\operatorname{argmin}} \sum_{\boldsymbol{\theta}, t, z \in \{x,y\}} p(\boldsymbol{\theta}) p(\boldsymbol{\theta} + \boldsymbol{\delta}_\theta) (s_z(\boldsymbol{\theta}, t) - \beta s_z(\boldsymbol{\theta} + \boldsymbol{\delta}_\theta, t + \delta_t))^2 \tag{2}$$

$$= \frac{\sum_{z \in \{x,y\}} [\boldsymbol{p}\boldsymbol{s}_z \circledast \boldsymbol{p}\boldsymbol{s}_z](\boldsymbol{\delta}_\theta, \delta_t)}{\sum_{z \in \{x,y\}} [\boldsymbol{p} \circledast \boldsymbol{p}\boldsymbol{s}_z^2](\boldsymbol{\delta}_\theta, \delta_t)}, \tag{3}$$

where $\circledast$ denotes the 3D correlation operator. Equation (3) can be quickly computed via adequately padded fast Fourier transforms. We also defined the correlation weight as

$$w(\boldsymbol{\delta}_\theta, \delta_t) = \frac{[\boldsymbol{p} \circledast \boldsymbol{p}](\boldsymbol{\delta}_\theta, \delta_t)}{\sum_{z \in \{x,y\}} p(\boldsymbol{\delta}_\theta, \delta_t)}. \tag{4}$$

Figure 2 presents the weighted auto-correlation of the $2\mathrm{D} + t$ slope cube introduced in Fig. 1, using 5 s of telemetry (5000 frames). Pure frozen flows measured on an infinite 2D plane and during an infinite amount of time would result in perfect Dirac translating at their corresponding wind speed. Nonetheless, because the measurements are spatially and temporally limited, this sharp signal expands in blobs surrounded by a structured background, while deviation from the frozen flow hypothesis will create a temporal decorrelation and expansion of the central spot. At least three of these correlation spots are strong enough to be easily trackable from one frame to another in the figure (dark red).

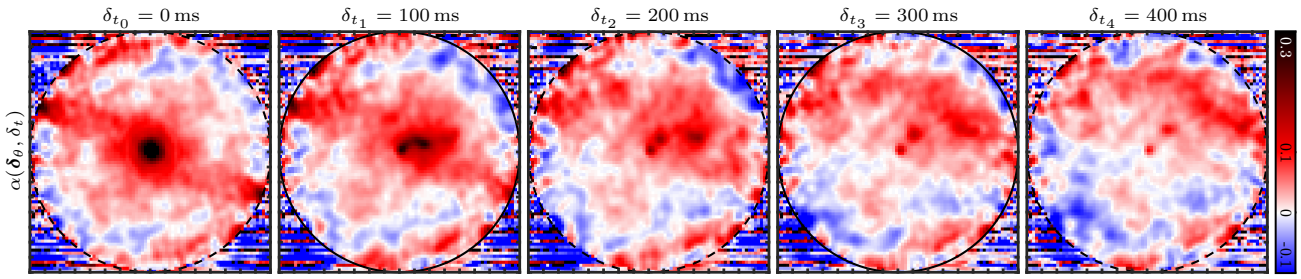

Figure 2. $2\mathrm{D} + t$ weighted auto-correlation of the pseudo-open loop of Fig. 1 using 5 s of closed loop telemetry (5000 frames). Multiple and distinct peaks corresponding to different frozen flow layers are clearly visible.

2.2 Frozen Flow Multi-Layer Estimator

Two varieties of methods exist to retrieve the different frozen layers from the auto-correlation cubes $\alpha(\boldsymbol{\delta}_\theta, \delta_t)$. The most straightforward method is to follow the correlation peaks [6, 15, 23]. Nonetheless, only the brightest ones can be tracked, the fainter being lost in the background dynamic structure mentioned above. Another method is to compute power spectrum density of different spatial frequencies [7, 18], in order to isolate the peaks from one another. Nonetheless, this is time consuming if a large variety of wind speeds must be scanned and peaks still corrupts each other. Both methods consequently suffer from the difficulty to disentangle the signal from the different layers.

In this work, we introduce a new approach to retrieve the different frozen layers and identify their parameters. It belongs to the first class of methods, following the layer directly in the auto-correlation cube. But instead of just following the brightest spots and remove it from the data to track the next one, and so on, our method fits both the spot and its associated structure via a 2D map $\alpha_\ell(\boldsymbol{\theta})$ of 2D velocity $\boldsymbol{v}_\ell$. The auto-correlation cube is consequently modelled as a linear combination of translating maps

$$\alpha(\boldsymbol{\delta}_\theta, \delta_t) \simeq \sum_{\ell=1}^{n_\text{layer}} \alpha_\ell(\boldsymbol{\delta}_\theta - \boldsymbol{v}_\ell \delta_t)\,. \tag{5}$$

Equation (5) is an analytical formulation of the problem. But at the end, it is solved on the discrete $2\mathrm{D} + t$ space given by the SH-WFS spatial resolution and the loop frame rate and can be expressed in terms of linear algebra. Noting $\boldsymbol{I}(\boldsymbol{v}_\ell)$ the linear 2D interpolation operator[†] from the 2D space $\boldsymbol{\theta}$ to the 3D space $(\boldsymbol{\delta}_\theta, \delta_t)$ for the velocity $\boldsymbol{v}_\ell$, the problem equivalently writes as

$$\boldsymbol{\alpha} \simeq \sum_{\ell=1}^{n_\text{layer}} \boldsymbol{I}(\boldsymbol{v}_\ell) \cdot \boldsymbol{\alpha}_\ell\,. \tag{6}$$

Inverting Eq. (6) is done following the algorithm Algorithm 1.

Algorithm 1 Iterative greedy algorithm to fit frozen flow layers $\{\boldsymbol{\alpha}_\ell\}$ in the auto-correlation cube $\boldsymbol{\alpha}$.

1: **for** $n_\text{layer} = \left[1, \cdots, n_\text{layer}^\text{max}\right]$ **do** ▷ Iteratively adding extra layers
2: **for** $\ell = \left\{n_\text{layer} \text{ and } \left[1, \cdots, n_\text{layer}^\text{max} - 1\right]\right\}$ **do** ▷ Loop on the layer, starting with the new one
3: $\boldsymbol{\alpha}_\ell^\text{res} \underset{\text{Eq. (7)}}{\leftarrow} \boldsymbol{\alpha} - \sum_{m=1, m\neq\ell}^{n_\text{layer}} \boldsymbol{I}(\boldsymbol{v}_m) \cdot \boldsymbol{\alpha}_m$ ▷ Residuals of ℓ^th-layer
4: $\boldsymbol{v}_\ell \leftarrow$ velocity of brightest peak in $\boldsymbol{\alpha}_\ell^\text{res}$ ▷ Wind speed of ℓ^th-layer
5: $\boldsymbol{\alpha}_\ell \underset{\text{Eq. (11)}}{\leftarrow} \left[\boldsymbol{I}^\mathrm{T}(\boldsymbol{v}_\ell) \cdot \boldsymbol{W} \cdot \boldsymbol{I}(\boldsymbol{v}_\ell)\right]^{-1} \cdot \boldsymbol{I}^\mathrm{T}(\boldsymbol{v}_\ell) \cdot \boldsymbol{W} \cdot \boldsymbol{\alpha}_\ell^\text{res}$ ▷ ℓ^th-frozen layer 2D model
6: $\forall \ell, C_{n,\ell}^2 \leftarrow \alpha_\ell(\boldsymbol{0})$ ▷ Layer strengths
7: $\{\boldsymbol{\alpha}_\ell\} \leftarrow$ sort $\{\boldsymbol{\alpha}_\ell\}$ with descending $C_{n,\ell}^2$ ▷ Sorting layers by strength
8: **return** $\left(\{\boldsymbol{v}_\ell\}, \{C_{n,\ell}^2\}, \{\boldsymbol{\alpha}_\ell\}\right)$ ▷ Returning wind speeds, strengths and correlation layers

The greedy algorithm adds new layers one by one, see, Line 1. For each new layer, the method fits the new layer before refining again the previously fitted layers, see Line 2. Putting back the old layers in the fit permits to iteratively clean the 2D maps from potentially cross-corruption with other layers that are later included in the model.

[†]For each output of 3D coordinates $(\boldsymbol{\delta}_\theta, \delta_t)$, the input is linearly interpolated on the 2D position $\boldsymbol{\delta}_\theta - \boldsymbol{v}_\ell \delta_t$.

To fit a layer, first, the residuals of the other known layers are computed, see Line 3:

$$\boldsymbol{\alpha}_\ell^{\text{res}} = \boldsymbol{\alpha} - \sum_{m=1, m\neq\ell}^{n_{\text{layer}}} \boldsymbol{I}(\boldsymbol{v}_m) \cdot \boldsymbol{\alpha}_m \,. \tag{7}$$

Doing so enhances the remaining layers that are not fitted yet and their correlation peak.

The velocity $\boldsymbol{v}_\ell$ of the brightest spot in these residuals is fitted, see Line 4. This spot is modelled as a Gaussian pattern whose parameters (amplitude, size, offset) are fitted on the first frame imposing its position[‡] at $\mathbf{0}$. Keeping the size of spot fixed, its position $\boldsymbol{\delta}_\theta(\delta_t)$ is followed frame after frame on a region of interest of 7 pixels centred on $\boldsymbol{\delta}_\theta(\delta_{t-1})$. Along with its position, its amplitude and offset are also updated at each frame. Indeed, fitting the amplitude permits accounting for the layer decorrelation while fitting its pedestal makes it more robust to the presence of background structures from other layers.

Once the velocity of the layer is estimated, the global 2D correlation map $\boldsymbol{\alpha}_\ell$ of this layer is reconstructed, see Line 5. This is done by approximating the residual cube or Eq. (7) as the realisation of a single frozen flow map

$$\boldsymbol{\alpha}_\ell^{\text{res}} \simeq \boldsymbol{I}(\boldsymbol{v}_\ell) \cdot \boldsymbol{\alpha}_\ell \,. \tag{8}$$

This equation is inverted, accounting for the correlation weight of Eq. (4) to give more confidence to the positions in $\boldsymbol{\alpha}$ that are derived from large pupil overlaps:

$$\tilde{\boldsymbol{\alpha}}_\ell = \underset{\boldsymbol{\alpha}_\ell}{\text{argmin}} \, \|\boldsymbol{\alpha}_\ell^{\text{res}} - \boldsymbol{I}(\boldsymbol{v}_\ell) \cdot \boldsymbol{\alpha}_\ell\|_{\boldsymbol{W}} = \underset{\boldsymbol{\alpha}_\ell}{\text{argmin}} \, [\boldsymbol{\alpha}_\ell^{\text{res}} - \boldsymbol{I}(\boldsymbol{v}_\ell) \cdot \boldsymbol{\alpha}_\ell]^{\text{T}} \cdot \boldsymbol{W} \cdot [\boldsymbol{\alpha}_\ell^{\text{res}} - \boldsymbol{I}(\boldsymbol{v}_\ell) \cdot \boldsymbol{\alpha}_\ell] \tag{9}$$

$$= \underset{\boldsymbol{\alpha}_\ell}{\text{argmin}} \sum_{\boldsymbol{\delta}_\theta, \delta_t} w(\boldsymbol{\delta}_\theta, \delta_t)(\alpha_\ell^{\text{res}}(\boldsymbol{\delta}_\theta, \delta_t) - [\boldsymbol{I}(\boldsymbol{v}_\ell) \cdot \boldsymbol{\alpha}_\ell](\boldsymbol{\delta}_\theta, \delta_t)) \tag{10}$$

$$= \left[\boldsymbol{I}^{\text{T}}(\boldsymbol{v}_\ell) \cdot \boldsymbol{W} \cdot \boldsymbol{I}(\boldsymbol{v}_\ell)\right]^{-1} \cdot \boldsymbol{I}^{\text{T}}(\boldsymbol{v}_\ell) \cdot \boldsymbol{W} \cdot \boldsymbol{\alpha}_\ell^{\text{res}} \,, \tag{11}$$

where $\boldsymbol{W}$ is the diagonal matrix built from $\boldsymbol{w}$.

By definition, the turbulence strength of each layer is given by the intensity of the correlation peak, see Line 6:

$$C_{n,\ell}^2 = \alpha_\ell(\mathbf{0}) \,. \tag{12}$$

This is used to sort the different layers by descending order, see Line 7. The total number of layers $n_{\text{layer}}^{\max}$ to fit can either be a number fixed by the user or by using a stopping criterion on the minimal fitted turbulence strength $C_{n,n_{\text{layer}}}^2$.

The equivalent turbulence wind is then classically obtained by [11, 20]

$$v_0 = \frac{\left(\sum_{\ell=1}^{n_{\text{layer}}} C_{n,\ell}^2 |\boldsymbol{v}_\ell|^{5/3}\right)^{3/5}}{\left(\sum_{\ell=1}^{n_{\text{layer}}} C_{n,\ell}^2\right)} \,. \tag{13}$$

The normalisation by the sum of the C_n^2 is here to enforce their sum to be equal to 1, as it should be. Indeed, fitting a limited number of layers could lead to an underestimation of the total turbulence strength that must be compensated when computing v_0. Combined with the Fried's parameter r_0 fitted by the `AtmPerfMonitor` on the variances of the pseudo-open loop slope projected on Zernike modes, see Ref. [3], it is finally possible to derive the coherence time

$$\tau_0 = 0.314 \frac{r_0}{v_0} \,. \tag{14}$$

3. RESULTS AND PERSPECTIVES

3.1 Disentangling Multiple Layers

Figure 3 shows the different 2D correlation maps $\boldsymbol{\alpha}_\ell$ obtained from the weighted auto-correlation cube $\boldsymbol{\alpha}$ of Fig. 2. Beyond the three obvious layer mentioned in Sec. 2.1, the model was able to retrieve 5 additional frozen flow correlation layers. It appears that the two first layers have a strong background signal, with values higher than the layers $\ell \geq 5$. This supports the fact that faint layers can only be retrieved after a correct removal of the 2D maps of the strongest layers, and not only their correlation peak [6]. Interestingly, the different estimated

[‡]By definition, for $\delta_t = 0$, the correlation spots of all layers are centred at $\boldsymbol{\delta}_\theta = \mathbf{0}$, see Fig. 2.

correlation maps are mostly free of cross-corruption. Only $\ell = 5$ and $\ell = 6$ layers show trails due to stronger neighbouring layers. This shows that the greedy algorithm where the layers are refined again at each step is effective at disentangling the different layers. Except for $\ell = 4$ and $\ell = 7$, all layers have different speeds and directions supporting the hypothesis of frozen flow layers carrying most of the energy. Indeed, non-frozen flow would decorrelate with time, deforming the correlation peak. This is potentially the case for the layers $\ell = 4$ and $\ell = 7$ that present similar 2D velocities: to account for the layer variability, the model must fit two close frozen layers whose slight velocity differences mimic decorrelation.

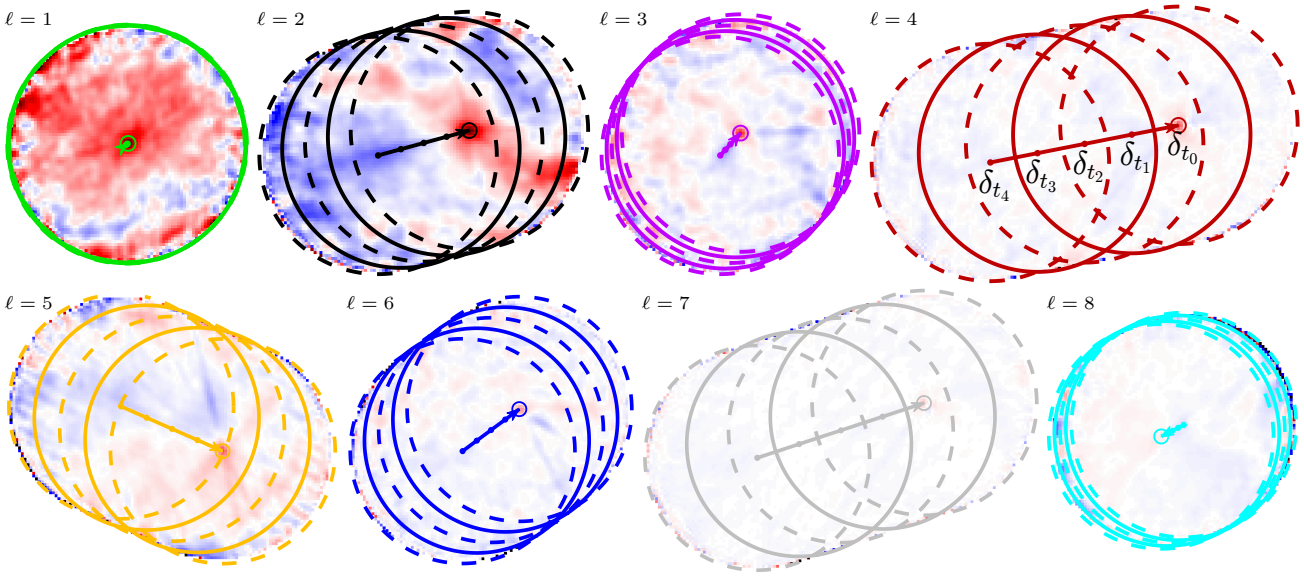

Figure 3. 2D frozen auto-correlation maps $\boldsymbol{\alpha}_\ell$ of the eight reconstructed layers from the cube $\alpha(\boldsymbol{\delta}_\theta, \delta_t)$ of Fig. 2. The circles emphasise the time stamps displayed in Figs. 2 and 5.

Figure 4 displays the turbulence profile estimated by the method: $\left\{C_{n,\ell}^2\right\}$ and $\{|\boldsymbol{v}_\ell|\}$. By design, the layers are stored by decreasing strengths. Our method efficiently fits layers on a large range of wind speeds, from a few meters per second to more than $30\,\mathrm{m\,s^{-1}}$. This makes our method very efficient compared to power spectrum density approaches.

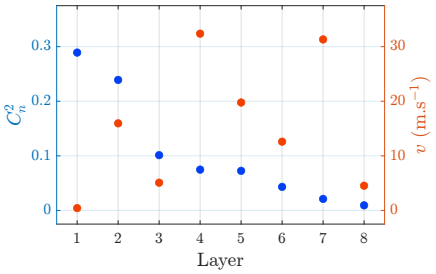

Figure 4. Estimated wind speed v_ℓ and C_n^2 of the eight reconstructed layers from the cube $\alpha(\boldsymbol{\delta}_\theta, \delta_t)$ of Fig. 2.

Figure 5 presents the residuals of the method for different numbers of fitted layers n_{layer}. They show how effective is the estimation and removal of full 2D layers. (I) This avoids fitting secondary peaks belonging to the same layer if only its main peak was removed. (II) By cleaning the background structures, this helps to reveal fainter moving layers. After the removal of the 2 first layers (second column), most of the background structures are gone: the third layer (purple) is enhanced, but also fainter peaks are now easily identifiable (orange, dark blue, red) whereas they were invisible in the full cube $\boldsymbol{\alpha}$.

3.2 Turbulence and Atmosphere Monitoring

In the previous section, we focused on a specific acquisition in NGS VIS (40×40 SH-WFS). In this section, we present results obtained during several nights across the different GPAO modes and using different UTs: during the VLTI science run of August 2025 when only the NGS modes of GPAO were available, during technical time

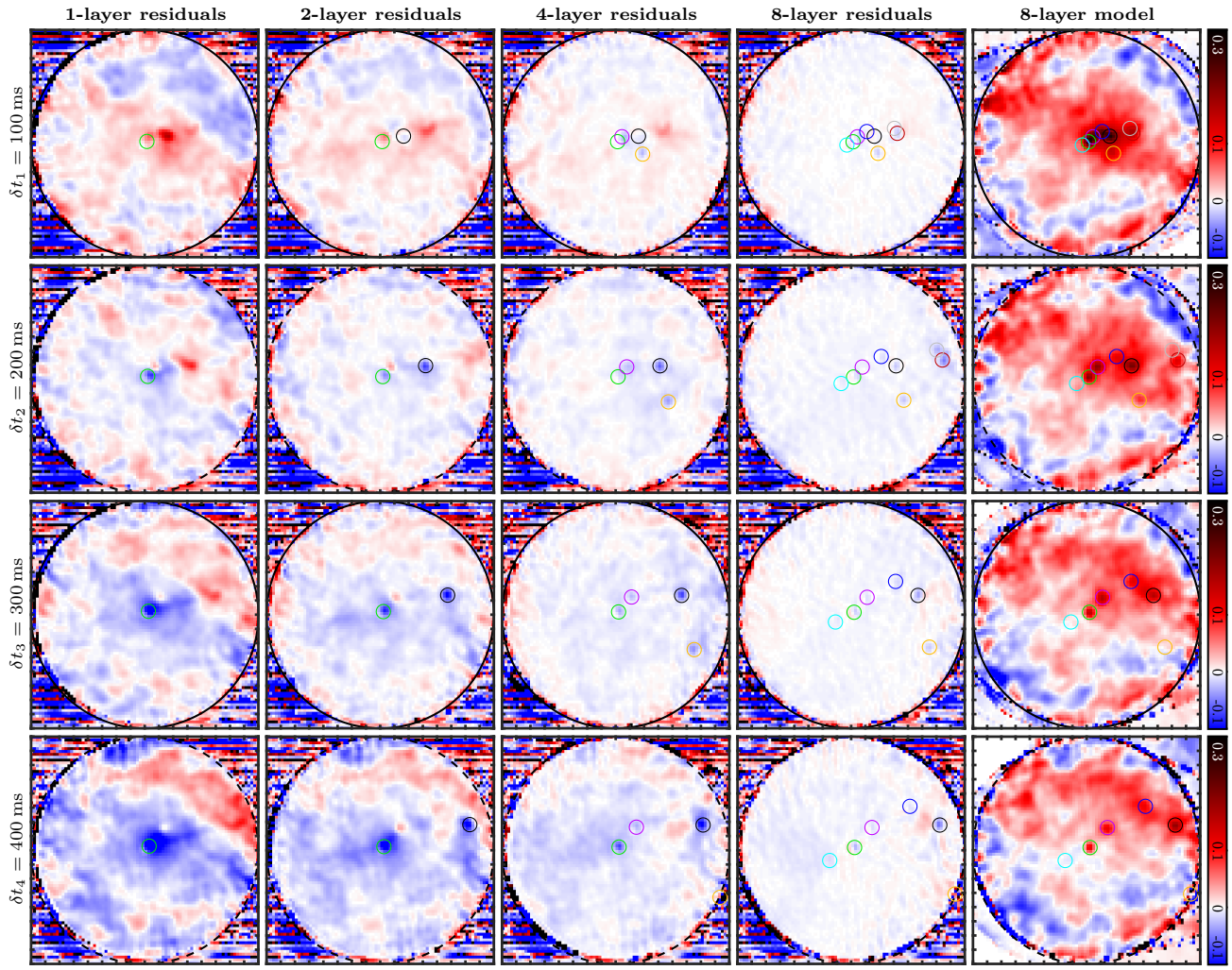

Figure 5. Residuals of our multi-layer frozen flow model for different number of layers and different times. The last column shows the total model and should be compared to the data of Fig. 2.

in July 2025 where the LGS mode of GPAO was during tests and compared with the performances of the NGS modes, and during the science verification of March 2026 at the end of the LGS mode commissioning on the four UTs.

Figure 6 presents the estimated equivalent wind speed v_0. For information, the wind speed measured by the DIMM is also shown (black). Let us note here that the DIMM logs the wind at 10 m and 30 m above ground. This is striking from the figure that this wind is obviously not the turbulent wind that the AO systems see and correct. In particular for the night of 2025-08-08 where the AO system was limited by the jet stream flow high in altitude. The different graphs show that all the GPAOs are in good agreement, following the same trends. It is also interesting that despite its low resolution, the 9×9 NGS IR SH-WFS manages to estimate wind speeds v_0 equivalent to the higher resolution 40×40 NGS VIS (2025-08-04 and 2025-08-07) or 30×30 LGS (2025-07-30) SH-WFSs. The technical nights of July 2025 were also a unique opportunity to test the impact of the LGS cone effect, with UT1 running on a NGS while UT4 was on its LGS: the curves are similar.

Finally, Fig. 7 shows the estimated coherence time τ_0 on the same nights. The DIMM also provides an estimation of τ_0. If our method globally follows the trends of the DIMM, there are some discrepancies. Small variations are expected as the DIMM generally does not point in the same direction as the UTs. Nonetheless, during the night of 2025-08-06, the estimate coherence time in NGS VIS seems very optimistic with values between 20 and 30 ms compared to 10 ms, which seems hard to believe. Looking back at Figs. 2 and 3, it is possible to see that the most important correlation peak is the one centred in $\boldsymbol{\delta}_\theta = \mathbf{0}$ and that it is barely moving. It is interpreted as the dome seeing, mainly made of boiling but not translating turbulence. From Fig. 4, its estimated strength reaches $C_n^2 \simeq 0.3$. Looking at Eq. (13), a strong dome seeing that is not discarded in the computation of the equivalent wind speed will artificially bias its estimate towards lower values. Or equivalently to artificially

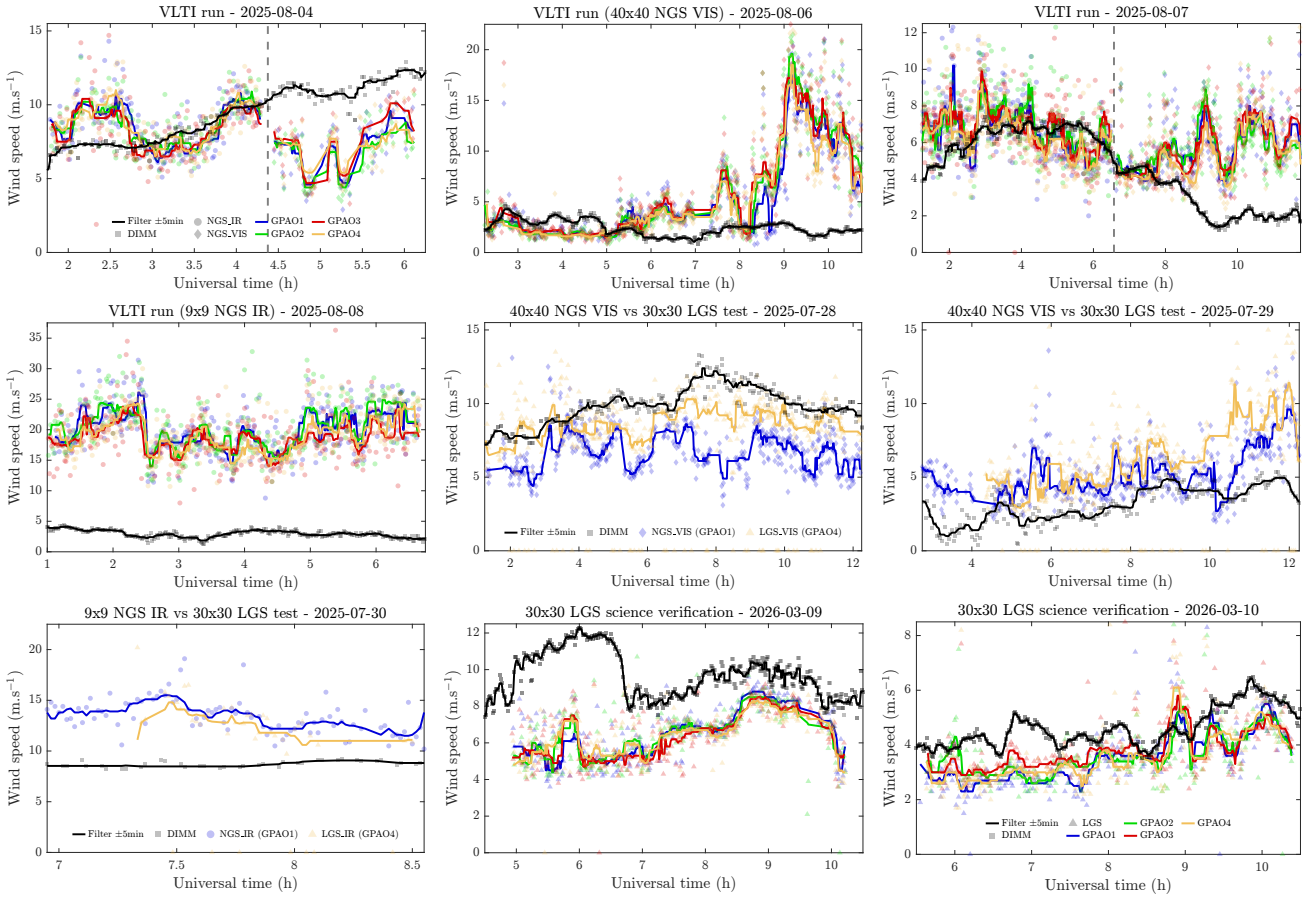

Figure 6. On-sky estimation of the equivalent wind speed v_0 with telemetry from the science run of August 2025 (operating 40×40 NGS VIS (diamonds) and 9×9 NGS IR (circles) modes), technical time of July 2025 (comparing 30×30 LGS (triangles) with NGS modes) and LGS science verification, compared to the DIMM (squares). The different colours emphasise the different GPAOs.

higher coherence time τ_0.

3.3 Wavefront Reconstruction: Towards AO Auto-Calibration and Predictive Control?

A quantitative multi-layer estimator opens several perspectives. We introduce some of them in this section.

3.3.1 Multi-layer wavefront reconstruction

Figure 8a shows a DM command re-shaped in 2D. When multiplied with the influence function of the GPAO PSIM model, see Ref. [3], one gets the membrane shape of Fig. 8b which corresponds to the wavefront that is corrected by the AO system. Now that the different wind speeds are estimated, it is possible to apply the same inversion of Eq. (11) but applied on this wavefront to retrieve the frozen flow turbulent screens crossing the pupil.

Figure 9 shows the different frozen screens that are estimated from 400 ms of telemetry. The full model and the quality of the residuals of Figs. 8c,d support the fact that the frozen flow approximation can explain most of the wavefront energy. The temporal residuals (not shown here) mainly present residual jitter that can be attributed to the telescope and system vibrations that are compensated by the AO system.

The different layers of Fig. 9 have a typical Kolmogorov structure that suggests that they are real and with a limited cross-corruption. Only the layer $\ell = 6$ seems to be an artificial drooling generated by the multi-layer estimator rather than a turbulent layer. This opens more perspectives regarding turbulence profiling from single conjugated AO[§] (SCAO). Indeed, it should be possible to fit the Fried's parameter r_0 of each of the layer and refine the anisoplanetic angle estimation.

[§]All GPAO modes are SCAO: the AO system locks the loop on a single star with a single WFS and only one DM conjugated with the entrance pupil corrects the turbulence. There is consequently no stereoscopic information.

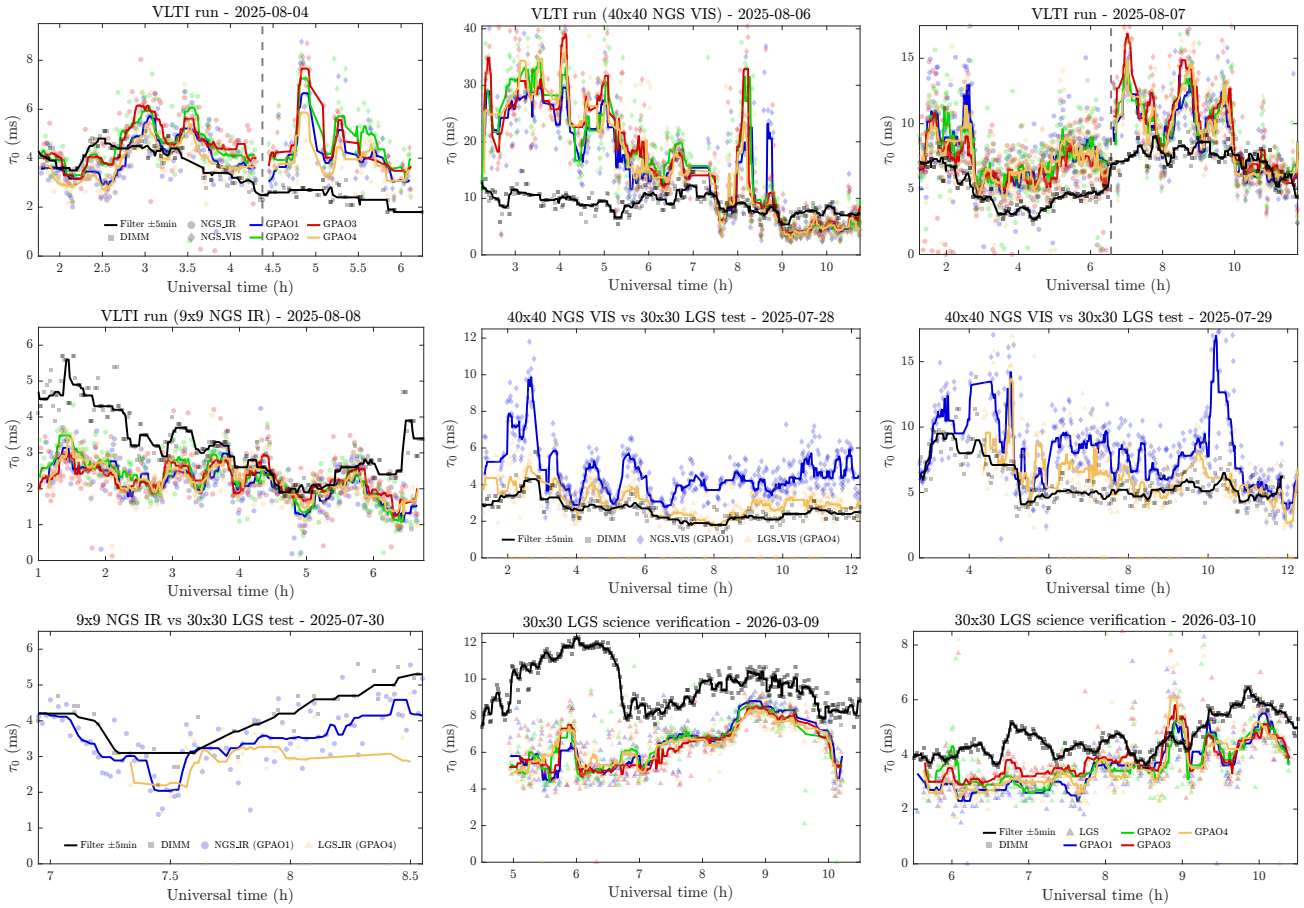

Figure 7. On-sky estimation of the coherence time τ_0. See caption of Fig. 6.

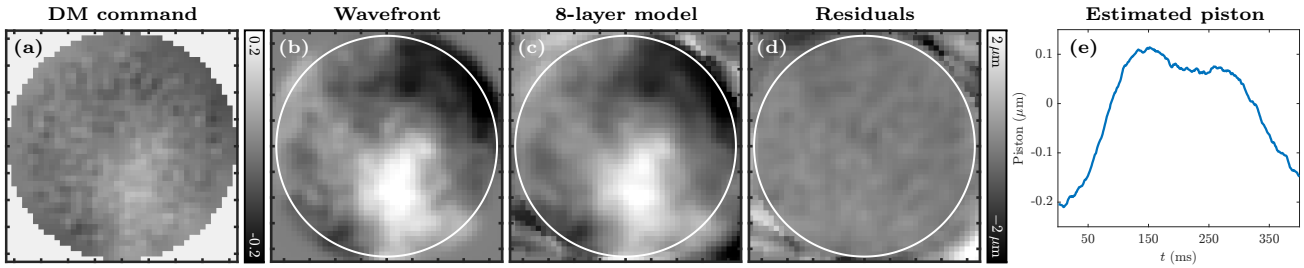

Figure 8. Multi-wavefront reconstruction from DM telemetry. Panel a: DM 2D command. Panel b: DM shape after applying the influence function model. Panel c: 8-layer wavefront model. Panel d: residuals. Panel f: estimated piston.

3.3.2 Predictive control

These findings have profound implications when it comes to AO predictive control. Indeed, most of AO system are based on integrators [9] or equivalent higher order controllers taking a given number of frames in the past (commands and measured slopes) to compute the next command [7, 16]. If most of the energy is indeed in frozen layers, an important part of the commands becomes predictable, something impossible to implement in this control framework. This pleads in favour of more physics-based approaches able to reconstruct the wavefront and translate it accordingly in the future to prepare the DM command, inspired for example from Fourier transform wavefront control [7, 19], but with a better knowledge of the wind speed, direction and strength.

But there is more. By design of the system, the SH-WFS is insensitive to the turbulence piston and the DM command is piston-free. To correctly model the wavefront passing in front the DM with frozen flow layers, it is necessary to add a piston component to the reconstruction, see 8e. This directly echoes the piston reconstruction experiment [P-Rex, 17, 23], aiming at predicting the piston evolution to improvement the performance of the fringe tracker of GRAVITY+. Nonetheless, this work was based on single layer frozen flow approximation. We have shown here that this approximation does not hold, with several strong turbulent layers generally measured by

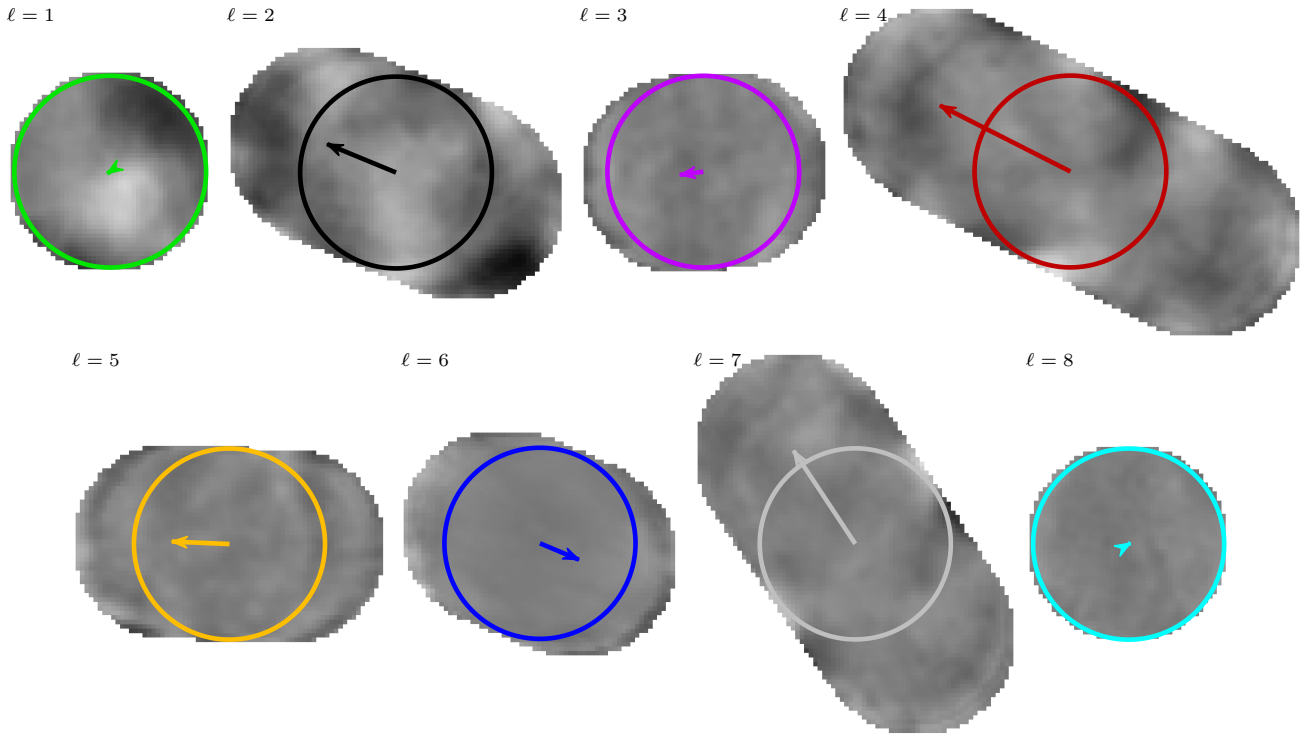

Figure 9. 2D frozen turbulence phase screens estimated from the DM telemetry of Fig. 8.

the GPAO systems. By providing an estimate of the different 2D wavefronts as well as their speed and direction, our method paves the way to piston prediction at small temporal scales[¶] that would help increase the exposure and thus the limiting magnitude of the fringe tracker.

Finally, let us mention that a better knowledge of the turbulence and its parameters can provide real time inputs to adapt the loop settings[‖] in operation as conditions evolve during the night. Such methods will benefit from using physics-based parameters quantitatively measured on-sky.

3.3.3 Mis-registration and system auto-calibration

As detailed in Ref. [3], GPAO uses a passive tracking of the lateral mis-registrations to auto-align the system on-the-fly to keep the DM and SH-WFSs aligned [4, 2]. This is a good example in operation of a complex system pre-figuring the future generation of extremely large telescopes (translating and rotating optics, pupil wobble, thermal dilations, mechanical stresses and deformations, segmented and evolving pupil): their complexity must be handled by auto-calibration strategies keep the systems closed to their optimal functioning point.

Measuring the mis-registration from closed loop telemetry is made complicated by frozen flows that bias the estimators [1, 13, 10]. The solution implemented for GPAO relies on the temporal correlation induced in the frequency space f by the cross-talk between the odd and even parts of the DM commands in presence of lateral mis-registrations [4, 2]. This correlation is proportional to the given spatial frequency $\boldsymbol{k}$ and the lateral error. This design limits the bias induced by a layer of velocity $\boldsymbol{v}_\ell$ by confining it to a sparse part of the measure around

$$f = \boldsymbol{k}_\ell^{\mathrm{T}} \cdot \boldsymbol{v}_\ell \,. \tag{15}$$

We show in Ref. [3] that indeed when running faster than 500 Hz the method keeps the system aligned to less than 25 % of a sub-aperture. Nonetheless, for slower frequencies and strong wind, the sparse signal falls in the peak of the correlation pattern indicating a mis-registration and the auto-alignment diverges. This is emphasised in Fig. 10 that shows the $\boldsymbol{k} + f$ correlations of the odd and even parts of the DM commands. The coloured lines are the solution of 15 for the different velocities fitted in Sec. 3.1. It is clearly visible that the lines match region of perfect correlation ± 1 which are characteristic of frozen flow layers, as described in Ref. [2].

[¶]The piston at large spatial and temporal scales cannot be measured as the model becomes totally degenerated for distances larger than the pupil diameter, leading to an underestimation of the piston since the wavefront with minimal norm will be reconstructed.

[‖]Such as the gain, the control matrix or the SH-WFS weight maps.

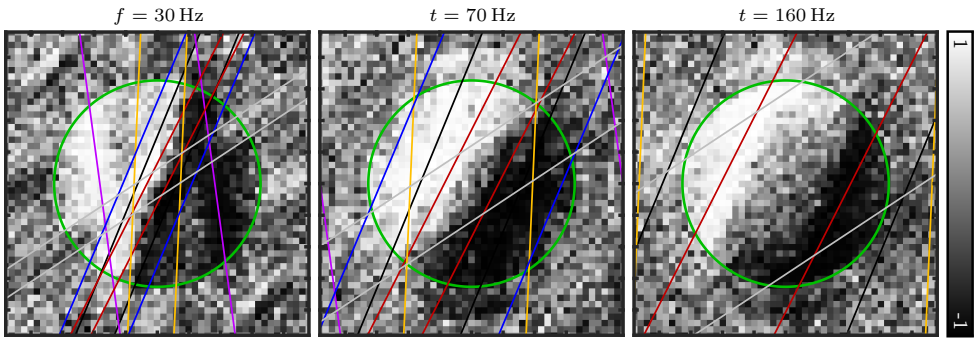

Figure 10. Impact of frozen flow layers in the spatio-temporal correlation of the GPAO mis-registration estimator. Each map is a slice of the $\boldsymbol{k} + f$ cube of correlation between the odd and even parts of the DM command. The lines correspond to the solution of the equation $f = \boldsymbol{k}_\ell^{\mathrm{T}} \cdot \boldsymbol{v}_\ell$ of each layer (colours of Fig. 9). The green circle emphasises the area of the controlled modes in the spatial frequency space $\boldsymbol{k}$.

Thus, the multi-layer estimator correctly locates the corrupted area. This paves the way towards debiasing techniques to reduce the impact of the wind in the mis-registration estimator. This could be by discarding the area of the $\boldsymbol{k} + f$ correlation cube impacted by the wind from the fit. But Fig. 15 tends to suggest that the corrupted area expands larger than the theoretical expected Dirac. A more promising solution would be to use the method developed to fit multiple layers to remove all the frozen flows from the DM commands and work on the residuals of Fig. 8d.

4. CONCLUSIONS

In this work, we presented a novel approach to extract the turbulence frozen flow parameters out of SCAO closed loop telemetry. The layers are fitted in the pseudo-open loop slope auto-correlation weighted by the pupil mask in which frozen layers produce well visible peaks. By fitting the correlation maps of each layer in their full complexity, our method solves the issues of standard approaches, in which multiple layers corrupt each other and hide fainter layers.

We applied our method on real on-sky data gathered with GPAO in different conditions and settings. Despite the variety of SH-WFSs resolution in GPAO, the method proved to be coherent throughout the different configurations, able to fit up to eight different layers in NGS VIS. If most of the time, the measurements compared well with the DIMM, we noticed some divergences. If the velocity of the different layers is correctly estimated, we think that the estimation of their strength is biased by dome seeing effects, artificially improving the estimated parameters.

We finished by investigating different perspectives for the method which has potential application in turbulence profiling, wavefront reconstruction and predictive control, or the de-biasing of AO loop monitors in charge auto-calibrating and optimising the system on-the-fly to adapt itself to the changing observing conditions.

The method should next be confronted to simulations to further demonstrate that it is quantitative and assess its limits in terms of number of layers or needed telemetry frames to extract the information. One of its main limitations is the intrinsic difficulty from SCAO data to retrieve the altitude of the different layers due to the lack of stereoscopic information. Some works proposed to use the SH-WFS intensities to relate the strength of the measured scintillation to the turbulence height [14, 22]. It could be interesting to know if these methods could be adapted to our frozen flow estimator to get the height of the different layers.

ACKNOWLEDGMENTS

This project has received funding from the European Union's Horizon 2020 research and innovation programme under grant agreement No 101004719 and has been supported by the french Agence Nationale de la Recherche through the ANR grant ANR-21-CE31-0011.

References

[1] C. Béchet, M. Tallon, and É. Thiébaut. "Optimization of adaptive optics correction during observations: algorithms and system parameters identification in closed-loop". In: *Adaptive Optics Systems III*. Ed. by B. L. Ellerbroek, E. Marchetti, and J.-P. Véran. Vol. 8447. Society of Photo-Optical Instrumentation Engineers (SPIE) Conference Series. July 2012, 84472C, p. 84472C. DOI: 10.1117/12.926574.

[2] A. Berdeu et al. “Estimation of the lateral mis-registrations of the GRAVITY$_+$ adaptive optics system. Perturbative method with open-loop modal correlation and non-perturbative method with temporal correlation of closed-loop telemetry”. In: *Astron. Astrophys.* 687, A157 (July 2024), A157. DOI: 10.1051/0004-6361/202449311. arXiv: 2407.07423 [eess.SP].

[3] A. Berdeu et al. “Auto-calibration and performance monitoring of GRAVITY+ Adaptive Optics system with physics-based methods and inverse problem approaches”. In: *AO4ELT8*. 2026.

[4] A. Berdeu et al. “Open loop calibration and closed loop non-perturbative estimation of the lateral errors of an adaptive optics system: examples with GRAVITY+ and CHARA experimental data”. In: *Adaptive Optics Systems IX*. Ed. by K. J. Jackson, D. Schmidt, and E. Vernet. Vol. 13097. Society of Photo-Optical Instrumentation Engineers (SPIE) Conference Series. Aug. 2024, 130970T, 130970T. DOI: 10.1117/12.3019843. arXiv: 2410.06569 [eess.SP].

[5] R. Dembet. “VLT Projects: GRAVITY+ RTC design”. In: *RTC4AO Workshop*. 2023.

[6] Z. Du et al. “Estimating atmospheric wind speeds from Gemini planet imager AO telemetry”. In: *Adaptive Optics Systems IX*. Ed. by K. J. Jackson, D. Schmidt, and E. Vernet. Vol. 13097. Society of Photo-Optical Instrumentation Engineers (SPIE) Conference Series. Aug. 2024, 130974E, 130974E. DOI: 10.1117/12.3020607.

[7] J. Fowler, M. A. M. Van Kooten, and R. Jensen-Clem. “Battle of the predictive wavefront controls: comparing data and model-driven predictive control for high contrast imaging”. In: *Adaptive Optics Systems VIII*. Ed. by L. Schreiber, D. Schmidt, and E. Vernet. Vol. 12185. Society of Photo-Optical Instrumentation Engineers (SPIE) Conference Series. Aug. 2022, 1218582, p. 1218582. DOI: 10.1117/12.2629521. arXiv: 2208.00984 [astro-ph.EP].

[8] E. Gendron and P. Léna. “Single Layer Atmospheric Turbulence Demonstrated by Adaptive Optics Observations”. In: *Astrophys. Space Sci.* 239.2 (Sept. 1996), pp. 221–228. DOI: 10.1007/BF00645776.

[9] Gravity+ Collaboration et al. “First light for the GRAVITY+ Adaptive Optics: Extreme adaptive optics for the Very Large Telescope Interferometer”. In: *Astron. Astrophys.* 707, A115 (Mar. 2026), A115. DOI: 10.1051/0004-6361/202555666. arXiv: 2509.21431 [astro-ph.IM].

[10] C. T. Heritier. “Innovative Calibration Strategies for Large Adaptive Telescopes with Pyramid Wave-Front Sensors”. Theses. Aix Marseille Université, Nov. 2019. URL: https://theses.hal.science/tel-02390861.

[11] A. Kellerer and A. Tokovinin. “Atmospheric coherence times in interferometry: definition and measurement”. In: *Astron. Astrophys.* 461.2 (Jan. 2007), pp. 775–781. DOI: 10.1051/0004-6361:20065788. arXiv: astro-ph/0610207 [astro-ph].

[12] J. Kolb et al. “Calibration strategy of the AOF”. In: *Adaptive Optics Systems III*. Ed. by B. L. Ellerbroek, E. Marchetti, and J.-P. Véran. Vol. 8447. Society of Photo-Optical Instrumentation Engineers (SPIE) Conference Series. July 2012, 84472D, p. 84472D. DOI: 10.1117/12.926369.

[13] J. Kolb et al. “What can be retrieved from adaptive optics real-time data?” In: *Adaptive Optics Systems III*. Ed. by B. L. Ellerbroek, E. Marchetti, and J.-P. Véran. Vol. 8447. Society of Photo-Optical Instrumentation Engineers (SPIE) Conference Series. July 2012, 84475U, 84475U. DOI: 10.1117/12.926402.

[14] Y. Lai-Tim et al. “Cn2 profile characterization from wavefront sensing in moderate turbulence”. In: *Unconventional Imaging, Sensing, and Adaptive Optics 2025*. Ed. by J. J. Dolne, S. R. Bose-Pillai, and M. Kalensky. Vol. 13619. International Society for Optics and Photonics. SPIE, 2025, 136190J. DOI: 10.1117/12.3065744. URL: https://doi.org/10.1117/12.3065744.

[15] D. M. Levinstein et al. “Estimating effective wind speed from Gemini Planet Imager’s adaptive optics data using covariance maps”. In: *Adaptive Optics Systems VIII*. Ed. by L. Schreiber, D. Schmidt, and E. Vernet. Vol. 12185. Society of Photo-Optical Instrumentation Engineers (SPIE) Conference Series. Aug. 2022, 121855X, p. 121855X. DOI: 10.1117/12.2629677. arXiv: 2211.16441 [astro-ph.IM].

[16] J. Nousiainen et al. “Power of prediction: spatiotemporal Gaussian process modeling for predictive control in slope-based wavefront sensing”. In: *Journal of Astronomical Telescopes, Instruments, and Systems* 10, 039001 (July 2024), p. 039001. DOI: 10.1117/1.JATIS.10.3.039001. arXiv: 2406.18275 [astro-ph.IM].

[17] S. Perera et al. “Piston Reconstruction Experiment (P-REx) - II. Off-line performance evaluation with VLTI/GRAVITY”. In: *Mon. Not. R. Astron. Soc.* 511.4 (Apr. 2022), pp. 5709–5717. DOI: 10.1093/mnras/stab3813.

[18] L. Poyneer, M. van Dam, and J.-P. Véran. “Experimental verification of the frozen flow atmospheric turbulence assumption with use of astronomical adaptive optics telemetry”. In: *Journal of the Optical Society of America A* 26.4 (Mar. 2009), p. 833. DOI: 10.1364/JOSAA.26.000833.

[19] L. A. Poyneer, B. A. Macintosh, and J.-P. Véran. "Fourier transform wavefront control with adaptive prediction of the atmosphere". In: *Journal of the Optical Society of America A* 24.9 (Jan. 2007), p. 2645. DOI: 10.1364/JOSAA.24.002645.

[20] F. Roddier. "The effects of atmospheric turbulence in optical astronomy". In: *Progess in Optics* 19 (Jan. 1981), pp. 281–376. DOI: 10.1016/S0079-6638(08)70204-X.

[21] P. Shchekaturov. "VLT Projects: SPARTA Upgrade". In: *RTC4AO Workshop*. 2023.

[22] J. Voyez et al. "Accurate measurement of Cn2 profile with Shack-Hartmann data". In: *Adaptive Optics Systems III*. Ed. by B. L. Ellerbroek, E. Marchetti, and J.-P. Véran. Vol. 8447. Society of Photo-Optical Instrumentation Engineers (SPIE) Conference Series. July 2012, 844759, p. 844759. DOI: 10.1117/12.925356. arXiv: 1207.4581 [astro-ph.IM].

[23] F. Widmann, J.-U. Pott, and S. Velasco. "P-REx: The Piston Reconstruction Experiment for infrared interferometry". In: *Mon. Not. R. Astron. Soc.* 475.1 (Mar. 2018), pp. 1224–1237. DOI: 10.1093/mnras/stx3306. arXiv: 1712.07716 [astro-ph.IM].